Hybrid GNSS/INS/UWB Positioning for Live Demonstration Assisted Driving

Monica Navarro[1], Javier Arribas[1], Jordi Vilà-Valls[2], Jordi Casademont[3], Anna Calveras[3] and Marisa Catalán [4]

***Abstract*— In Cooperative Intelligent Transport Systems, assisted or autonomous driving precise and reliable positioning and navigation is a key feature. This contribution presents experimental results from a pilot demonstration involving different stakeholders for assisted driving in smart city scenario. A low-cost multi-sensor fusion positioning prototype integrating GNSS, INS and UWB measurements, with communication capabilities has been integrated into a 5G communication architecture to test real-time positioning and communication capabilities in delay constraint/safety applications. A description of the prototype and experimental performance results are provided.**

I. Introduction

Location and positioning capabilities are features that have become a must in current and future location based services. Accurate and reliable positioning solutions have been extensively considered in the context of Cooperative Intelligent Transport Systems (C-ITS) [1], [2] and more recently for assisted and autonomous driving [3]. Among the different technologies Global Navigation Satellite Systems (GNSS) is the technology of choice for outdoor positioning, because of its accuracy and reliability at low cost and because it provides a global reference of user position. However, there are scenarios where either GNSS does not provide the required accuracy, not at least with low cost mass market receivers, or experience a denial of service event, such in tunnels, or urban canyon locations. A wide range of different technologies exist to complement, improve or extend the service capabilities provided by GNSS, ranging from dedicated sensors such as radars, lidars or cameras to available communication systems such as the specifically developed short range communications standard (ITS-G5) for C-ITS or general purpose cellular communication systems such as LTE or 5G. The scope of this work was to enhance GNSS-based solutions to improve assisted driving reliability, specially for scenarios where vulnerable road users (VRU) are involved, and to assess its performance in a real-time live demonstration. In particular, we target a low-cost prototype featuring accurate positioning and communication capabilities, to be hosted in the bicycle, i.e., the VRU in this scenario. Although this contribution focuses on the positioning solution, a general description of the overall demonstration and integration work is provided. The overall system elements and infrastructure is provided in Figure 1. The goal of the demonstration was to integrate and test different features of 5G networks and services. In particular, we target the integration of the accurate positioning device, which provided real-time positions of the bicycle through standard CAM messages to the cellular network, which delivered the Cooperative Awareness Messages (CAM) to the car. A warning protocol dealing with the vehicles position and car driver interface was specially developed for the demonstration. The communication between the cellular operator and the car took place through a real Multi-access Edge Computing (MEC) deployment close to the base station. The rest of the paper is organized as follows:

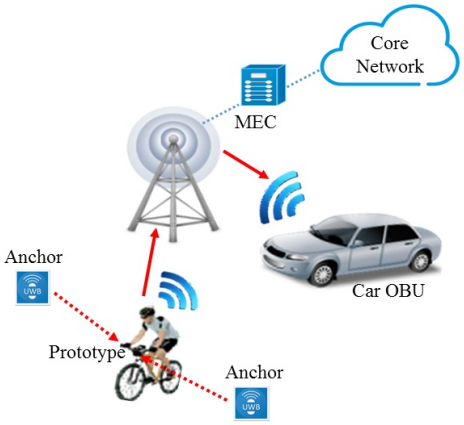

Fig. 1: System infrastructure elements involved in the demonstration.

Section II describes the system elements and scenario set-up for the demonstration, Section III introduces the prototype and the multi-sensor fusion algorithm; real-time performance is analysed in Section IV, followed by conclusions.

II. Scenario Description

An illustrative example of the urban scenario where the measurement campaign and demonstration took place is shown in Fig. 2 and 3. The bike rider trajectory started from the bike location depicted in Fig. 3, where details of the bike lane with respect to kerb, parking lane and the road can be appreciated. The latter drove on the left hand-side of the parking lane, with scarce visibility of the cyclist. In Fig. 2,

[1]M. Navarro and J. Arribas are with Centre Tecnològic de Telecomunicacions de Catalunya (CTTC), Castelldefels, Spain. [2]J. Vilà-Valls is with Institut Supérieur de l'Aéronautique et de l'Espace (ISAE-SUPAERO), University of Toulouse, France. Prior to join ISAE-SUPAERO in 2019 he was with CTTC, were he participated in the present work. [3]J. Casademont and A. Calveras are with Universitat Politècnica de Catalunya and i2CAT Foundation;[4] are with i2CAT Foundation; E-mails: {monica.navarro,javier.arribas}@cttc.es, jordi.vila-valls@isae.fr, jordi.casademont@upc.edu,anna.calveras@entel.upc.edu, marisa.catalan@i2cat.net.

the yellow circle marks two of the anchor positions. Both the car and the bicycle entered the roundabout from the left hand side of the picture. The pedestrian and bicycle crossing at one edge of the roundabout was the chosen location as a representative scenario with poor visibility between the car and the VRU. The specific location though was the result of a trade-off between local authorities and the need to find a challenging scenario for the demonstration goals. An overview of the street map, anchor locations (red squares) and target trajectory are shown in Fig. 10.

Fig. 2: Location: bicycle and car entering the roundabout from the left.

Fig. 3: Location: start of bike rider, from dedicated bike lane. Cars are allowed to park along the street, left to the bike lane.

The position of the anchor nodes were accurately referenced by a professional topographer. A total of eight anchors were placed in strategic positions along the relevant streets where the demonstration took place. It comprised a straight street with a separate bike line on the right-hand side along the bicycle direction, entering a roundabout with frequent traffic including large to medium logistic trucks, cars, emergency vehicles and buses.

The reference system was the standard UTM ETRS89 fus 31N with the following basis for the topographic elevation and anchor nodes. The attainment of UTM coordinates was performed by means of a GPS (Leica 1250) in static mode connected to the Cartographic Institute of Catalunya (ICGC) via Virtual Reference Station (VRS) network. Static observations were taken on stick and tripode for more than 10 minutes for each point. Afterwards, the basis adjustment was made on post-processing making use of the closest ICGC permanent stations. This methodology provides a stable reference network, preventing from error propagation from point to point measurements. The topographic elevation was then carried out using a total station with and angular accuracy of 3"(Trimble 5603 DR200), obtaining the UTM coordinates specified in Table II. Finally, since the prototype employs the reference system WGS84, anchors' UTM coordinates were transformed into WGS84 coordinates (longitude λ, latitude Φ and orthometric height H) using the LeicaGeo Office application. The coordinates are specified in III.

TABLE I: Basis for the topographic elevation in UTM ETRS89

Basis ID	X-coordinate	Y-coordinate	Z-coordinate
ST1	426634.859	4577726.817	5.590
ST2	426588.171	4577706.858	5.405
ST3	426542.035	4577664.409	6.075
ST4	426491.254	4577655.253	5.907
ST5	426503.307	4577610.796	6.098
H333	426510.685	4577644.228	6.089

TABLE II: Anchors topographic elevation in UTM ETRS89

Anchor ID	Hex. ID	X-coord.	Y-coord.	Z-coord.
1	6EC1	426468.775	4577670.042	8.432
2	6EBB	426478.791	4577649.907	7.963
3	7331	426497.813	4577640.361	8.203
4	6EBC	426495.282	4577661.620	7.969
5	6ECD	426509.656	4577653.800	8.064
6	6EC7	426536.462	4577675.084	8.060
7	6EBE	426560.818	4577675.956	8.409
8	7335	426584.669	4577706.956	7.460

TABLE III: Anchors WGS84 coordinates

Anchor ID	Longitude, λ	Latitude, Φ	Height, H
1	2º 7' 15.82116"	41º 20' 49.81354"	8.432
2	2º 7' 16.26089"	41º 20' 49.16398"	7.963
3	2º 7' 17.08351"	41º 20' 48.86071"	8.203
4	2º 7' 16.96534"	41º 20' 49.54918"	7.969
5	2º 7' 17.58721"	41º 20' 49.30035"	8.064
6	2º 7' 18.73132"	41º 20' 49.99926"	8.060
7	2º 7' 19.77891"	41º 20' 50.03553"	8.409
8	2º 7' 20.79164"	41º 20' 51.04850"	7.460

The anchors deployed along the city urban furniture and the tag mounted on the bicycle prototype, are radino32 UWB devices [4] which integrate the DecaWave DW1000 chip. For the anchors we used the waterproof enclosed version with an integrated antenna, whereas for the tag we used the version with SMA antenna connection. This configuration facilitated a suitable placement of the different antennas present in the prototype: the GNSS, the UWB and the

LTE antennas. In particular, it is recommended to allow for sufficient distance between the UWB antenna and the LTE dongle to avoid interference. In the final configuration, depicted in Fig. 6, they were place at the two extremes of the plastic enclosure. The GNSS antenna was placed on the top of the enclosure, facing the open sky. The selected UWB device provides a firmware that allows self-synchronization of the network, which was configured for a single tag, which delivered distance measurements based on the Two-way-ranging (TWR) protocol [4]. Radino32 firmware computes the Time-of-Flight (ToF),

$$\text{ToF} = (\Delta_1 - \Delta_2 + \Delta_3 - \Delta_4)/4$$

with $\Delta_1 = T_{RR} - T_{SP}$, $\Delta_2 = T_{SR} - T_{RP}$, $\Delta_3 = T_{RF} - T_{SR}$ and $\Delta_4 = T_{SF} - T_{RR}$. at the anchors and reports it back to the tag as illustrated in Fig. 4. The ranging phase

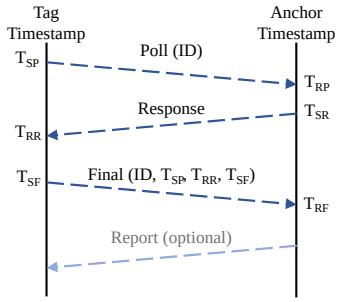

Fig. 4: Radino32 TWR protocol messages.

involves messages, Poll, Response, and Report. There is an initial discovery phase which transmits a Blink message. The discovery phase takes about 15 ms, whereas the minimum time delay between ranging measurements is 10 ms. These specifications comply with the velocity and accuracy requirements of the pilot demonstration[1]. The radino32 devices were configured to the parameter values shown in Table IV in order to comply with range (>100m), latency, ranging measurements frequency and power consumption requirements.

TABLE IV: UWB device configuration

Transmit power	33.5 dBm
Channel	4 ($f_c = 3993.6$ MHz)
Data transmission rate	110 kbps
Pulse Repetition frequency (PRF)	64 MHz
Preamble length	1024 symbols
Preamble code	17
Short address	directly read from EEPROM memory

[1]For speeds bellow 50 km/h these delays are equivalent to 15-20 cm displacement

(a) a (b) b

Fig. 5: Detail of the UWB anchor (yellow circle indicates the center for the reference position). Mounting of prototype in bicycle.

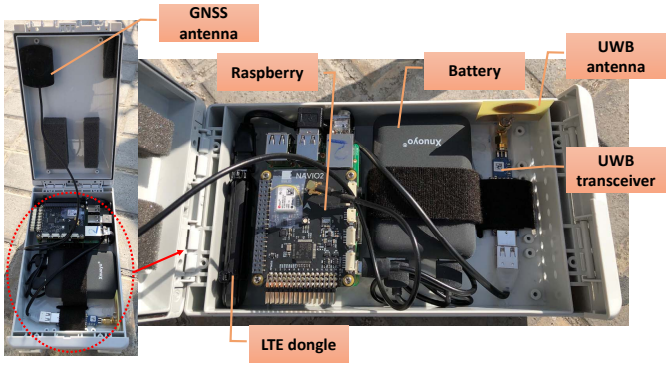

Fig. 6: Mounting of prototype in bicycle.

III. Low-cost Hybrid Positioning Prototype

In this work, the positioning prototype introduced in [5], and enhanced with UWB cooperative distance measurements in [6], was modified to integrate low-cost GNSS receivers that provide only Position, Velocity and Time (PVT) estimations. The prototype was also adapted to operate with a different UWB device, configured to deliver only ranging measurements not positions. This choice was motivated to allow for a lighter infrastructure deployment with a less dense network of UWB anchors and network configuration requirements.

A. Multi-sensor Fusion Algorithm

The selected algorithm is based on the strapdown INS equations [7]. More specifically, the data fusion algorithm performs a loose integration between the GNSS receiver and IMU sensors and a tight integration between UWB sensors and IMU sensors. The selection was motivated from practical reasons: one the one hand, the loose GNSS/INS fusion does not require pseudoranges measurements from the GNSS receiver which are not always available in COTS GNSS receivers. With this approach it is straight forward to replace the current GPS receiver used in the prototype [6] with any other commercial GNSS receiver without the need to modify the fusion algorithm. On the second hand, the tight range measurements integration allows for a simpler infrastructure deployment, as well as reduces constraints in the HW implementation of the sensor fusion algorithm, with respect to the vehicle speed. Especially in the configuration of the UWB anchors network. Furthermore, a tight integration of

UWB distance measurements avoids the implementation of an standalone UWB positioning solver, as well as reduces the minimum number of nodes in range for each new observation to be fused.

The complete mathematical description of the loose fusion algorithm and INS strapdown equations can be found in [7]. In the Annex we reproduce the state space and transition model with an unified notation for ease of the description of the proposed algorithm. To include the range measurements provided by the UWB nodes, the loose GNSS/INS state-space model is modified by including an extra observation into the innovation vector.

The following aspects were considered:

- The number of UWB range measurements available depends on the number of anchors in view, then, both the innovation vector and measurement matrix dimensions are time-varying.
- To obtain the INS-based distances to the different anchor nodes, a prediction block is included, which needs the set of anchor nodes' positions.
- With respect to standard tight integration architectures, there is no need to estimate the system clock offset because UWB measurements are synchronised with the GNSS clock (i.e., as IMU measurements).

The state to be tracked is again (2), and the innovation vector in this case is

$$\delta \mathbf{z}^e_{UG,k} = \begin{pmatrix} \hat{\mathbf{r}}^e_{eaG,k} - \hat{\mathbf{r}}^e_{eb,k} \\ \hat{\mathbf{v}}^e_{eaG,k} - \hat{\mathbf{v}}^e_{eb,k} \\ \delta \mathbf{z}^e_{\rho U,t} \end{pmatrix}, \tag{1}$$

with $\delta \mathbf{z}^e_{\rho U,t} = \left(\tilde{\rho}^1_U - \hat{\rho}^1_{uI}, \tilde{\rho}^2_U - \hat{\rho}^2_{uI}, \ldots, \tilde{\rho}^L_U - \hat{\rho}^L_{uI}\right)_t$. $\tilde{\rho}^j_U$ are the UWB range measurements to L anchors ($j = 1, \ldots, L$), and $\hat{\rho}^j_{uI}$, the corresponding INS-based prediction, which are obtained from both the INS position, $\hat{\mathbf{r}}^e_{eb,t}$, and known anchors' positions, $\hat{\mathbf{r}}^j_U$. The measurement matrix is,

$$\mathbf{H}^e_{UG,t} = \begin{pmatrix} \mathbf{0}_{m,3} & \mathbf{0}_{m,3} & -\mathbf{I}_3 & \mathbf{0}_{m,3} & \mathbf{0}_{m,3} \\ \mathbf{0}_{m,3} & -\mathbf{I}_3 & \mathbf{0}_{m,3} & \mathbf{0}_{m,3} & \mathbf{0}_{m,3} \\ \frac{\partial \mathbf{z}_{\rho U}}{\partial \delta \boldsymbol{\psi}^e_{eb}} & \mathbf{0}_{L,3} & \frac{\partial \mathbf{z}_{\rho U}}{\partial \delta \mathbf{r}^e_{eb}} & \mathbf{0}_{L,3} & \mathbf{0}_{L,3} \end{pmatrix}_{\mathbf{x}_t = \hat{\mathbf{x}}_{t|t-1}}$$

and $\mathbf{R}_{UG} = \text{diag}\left(\mathbf{R}_G, \mathbf{R}_{\text{UWB}}\right)$.

The prototype architecture, shown in Figure 7, remains the same as the one introduced in [6].

The additional information obtained by the UWB tag is injected to the Kalman filter as an independent measurement, that is as a new set of range estimates to a set of known static anchor nodes[2]. In the prototype this corresponds to the *cooperative receiver* module (Fig. 7). For each new radio range fusion the cooperative receiver module performs:

1) **Node range estimation** ($\hat{\rho}_c$): the UWB tag measures the range between the vehicle's antenna and the infrastructure anchors. The technology used by the equipment has no effect on the algorithm structure (e.g. could measure ranges to other vehicles) but should be used to adjust the filter parameters.
2) **Measurement covariance** ($\hat{R}_c$): every range measurement must have an associated covariance which can be derived using the received signal parameters. For this scenario, we consider the signal strength provided by the UWB tag.
3) **Node position estimation** ($\mathbf{r}^e_c$): In case of static nodes (or anchors), the node positions were provided using a pre-defined database (ECEF transformation of Table III coordinates).

[2]the algorithm could be directly extended to support dynamic anchors in a cooperative fashion

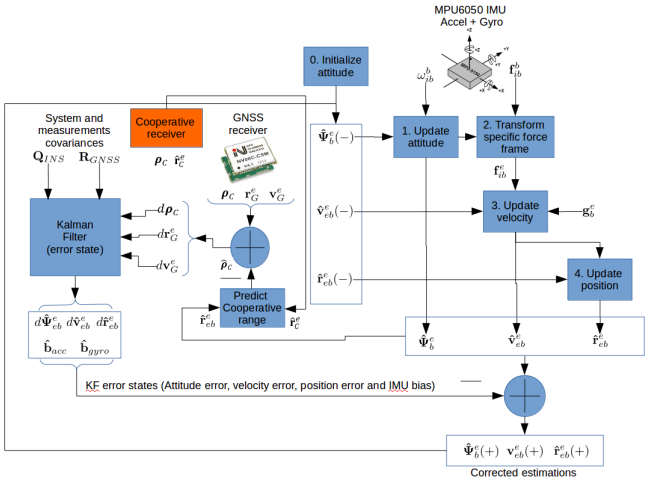

Fig. 7: Architecture of the hybrid GNSS/INS/UWB fusion.

IV. Performance Results

This section presents the results of the measurement campaign previous to the final demonstration [8]. We recorded several trajectories involving different dynamics and bike riders. In general the bike rider aimed at following the center of the bike lane in order to facilitate a visual reference in the map.

We first performed a calibration test to ensure the correct estimate of the anchors. The results of the test is shown in Fig. 8: (a) shows an overall plot of one realization of the UWB measured (logged) distance versus the reference distance obtained using the vector module from the anchor node position to the GNSS position estimation. Both distances were aligned in time and no relevant outliers were detected. However, observing in detail the measured distances when the bicycle is at the minimum distance from the anchor nodes, zoomed in (b), a measurement bias can be appreciated on some nodes in the order of 0.5 to 2.0 meters. The most probable cause of the measurement errors was the existing distance between the GNSS antenna, which was used as a reference *ground true* position for this test, and the UWB antenna, and the GNSS bias due to the ionospheric propagation delay, uncorrected in a low-cost, single-frequency receiver.

The only distance measurement quality indicator provided by the UWB device is the measured Received Signal Strength (RSS), shown in Fig. 9 (a) for the same experiment plotted in

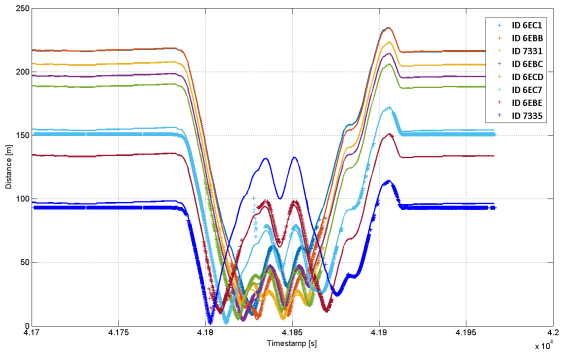

(a)

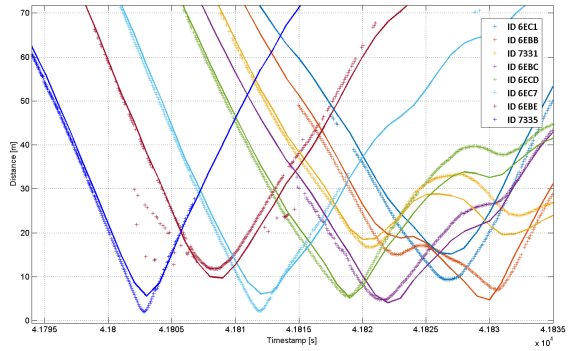

(b)

Fig. 8: Calibration check: Ranging measurements accuracy.

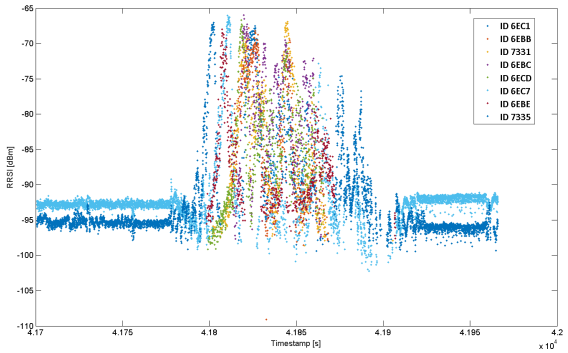

(a)

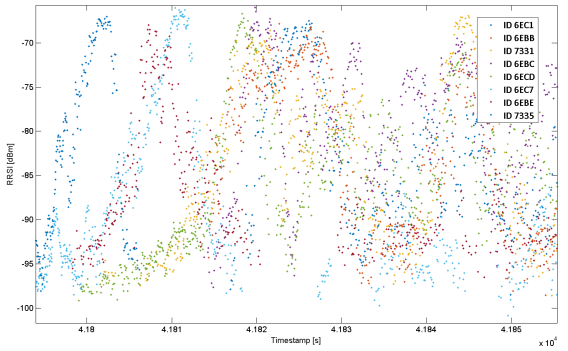

(b)

Fig. 9: Ranging Quality Indicator: Received Signal Strength (RSS).

Fig. 8; Fig. 9 (b) shows a detailed plot during the minimum distance to nodes. The RSS measures are aligned with the expected behavior, consequently they can be used to estimate the UWB measurement covariance matrix diagonals in the fusion algorithm. However, this indicator is not reliable to discard nodes which may be in NLOS or perform badly. This is the case of node 6EBE, placed beyond the car lane, which experience significant biases due to the multipath caused by the parked cars. This node was removed in the final configuration of the fusion algorithm. We shall remark that the node placement was not selected for optimal geometric dilution of precision (GDOP), but were constraint to available urban infrastructure.

We next present two bike trajectories, namely *bike ride #1* and *bike ride #2* with similar trajectories but stressing the dynamics for the first one. Both in terms of speed in the roundabout and bike tilts on the straight trajectory. The comparison of the different sensor fusion configurations are depicted in Fig. 10 and 11, respectively. In both cases a zoom near the pedestrian crossing and roundabout is also depicted, since it is the area selected for the assisted driving demonstration, with the larger number of UWB anchor nodes. The dotted green line indicates the trajectory output by the commercial GPS, the GNSS/INS fusion trajectory is represented by the dashed blue line, whereas the red solid line depicts the hybrid GNSS/INS/UWB fusion. Clearly in both experiments the 6EBE node was not providing reliable measurements (magenta line) due to NLOS condition and was removed from the fusion algorithm (the actual anchor remain operative). In both experiments the additional observations provided by the accurate UWB range measurements improved the trajectory estimate by the fusion algorithm. In particular, in the case of lower dynamics (Fig. 11) where the low cost IMU suffers from loss of accuracy in the attitude estimate. This effect can be appreciated in the following figures where the heading and velocity estimates are represented.

In the experiment we included a first stage where the bicycle remained static to facilitate calibration and detection of possible anomalies in the prototype. This period is clearly observed in Fig. 12 and 13 first and last part of the graph where the GPS (dashed green) in unable to estimate the heading because the vehicle is static. When fusing with the INS, the heading estimate improves but the convergence is slow, which can be observed in the heading estimate centered around 4.18 10^4 seconds for the GNSS/INS fusion (blue), with respect GNSS/INS/UWB fusion (red) which includes in the fusion algorithm the course over ground (COG) estimate provided by the GPS (green). Heading estimation can be improved, specially when the vehicle experiences low dynamics, with the integration of a magnetometer.

The improvement is also appreciated in the estimation of the velocity (Fig. 14 and 15). Improving the estimation of

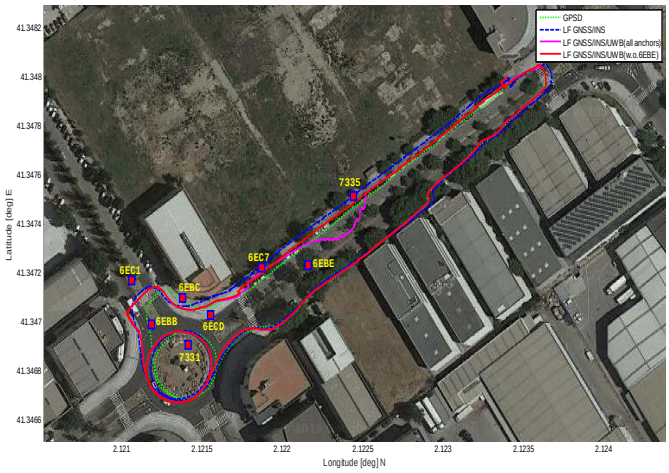

(a)

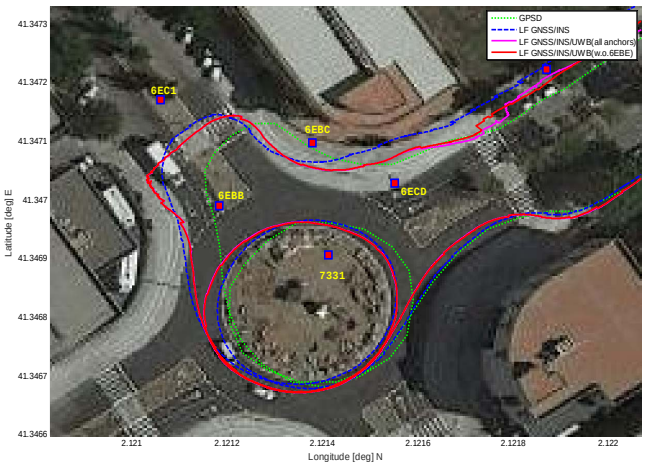

(b)

Fig. 10: Tracking of cyclist trajectory applying sensor fusion algorithm for bike ride # 1 (higher dynamics).

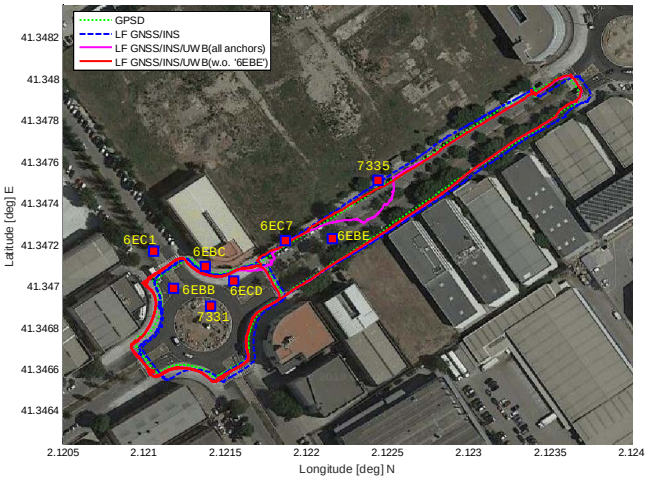

(a)

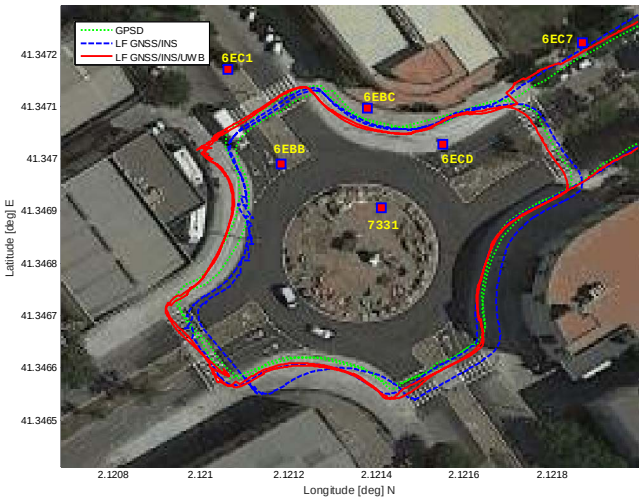

(b)

Fig. 11: (a)Tracking of cyclist trajectory applying sensor fusion algorithm for bike ride #2, (b) Zoom roundabout.

the heading and the velocity translates to an improvement in the positioning estimate. In Fig. 14 and 15 we can also appreciate the difference in the velocity magnitude, the *bike ride #1* exceed the 20m/s in most of the trajectory, while *bike ride #2* remain bellow most of the time.

The pilot showcase was deployed during the Barcelona's Mobile World Congress 2019 to validate the capacity of the prototype to prevent from collisions between bicycles and cars. The car's main board of the prototype implemented the C-ITS protocol stack (Vanetza framework) and was configured to report location updates every 100 ms using CAM to MEC specifically deployed for the pilot. During the pilot demonstration the car enabled with an OBU, received the CAM messages and determined if there existed a potential collision danger. For this, a "danger zone" surrounding the car was defined. Accurate tracking, together with the ability to acquire and send this information in real-time (every 100 ms), was successfully tested over 3 days with more than 10 realisations every day.

Notice that the fusion filter parameters were calibrated previous to the final pilot demonstration, but remained fixed during the tens of independent experiment realisations. The prototype was on during more than 3 consecutive hours for each demonstration slot, without identifying any drift, or HW malfunctioning. A specific real-time display, independent from the car driving board, was developed to test the performance from a companion PC, connected by WiFi to the positioning prototype.

V. Conclusion

We have introduced a hybrid fusion algorithm, combining a loose integration of GNSS and INS measurements with a tight UWB range measurements to enhance GNSS based positioning in challenging scenarios. The solution has been developed and integrated into a real-time testbed using commercial equipment jointly with proprietary HW/SW components aiming at low-cost prototype for VRUs. Although the system has been tested for a bicycle user, it could be extended to other vehicles. Reliable and accurate positioning

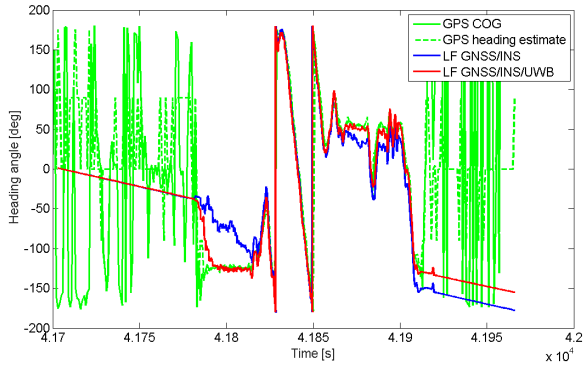

Fig. 12: Heading for bike ride #1.

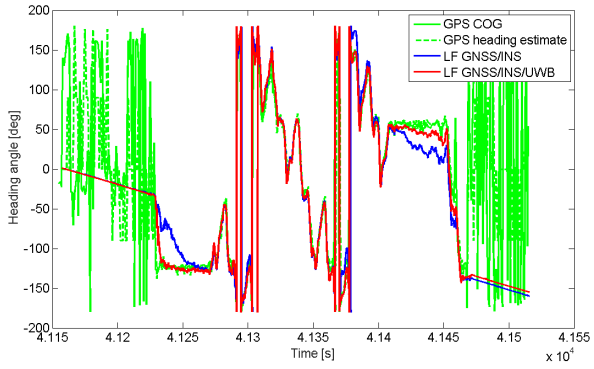

Fig. 13: Heading for bike ride #2.

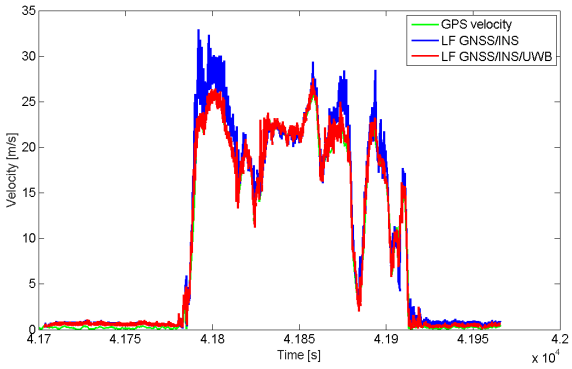

Fig. 14: Velocity for bike ride #1.

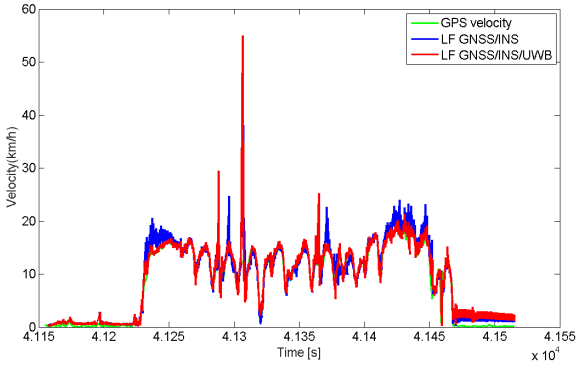

Fig. 15: Velocity for bike ride #2.

has been tested over a commercial cellular network adapted to include the MEC component achieving lane-accuracy at the target latency of few miliseconds. One of the features of the prototype is that it can operate in standalone mode when no additional infrastructure is available (UWB anchors) and take advantage in a seamless integration whenever the smart city infrastructure is available.

Annex - Loose GNSS/INS Fusion

The loose GNSS/INS fusion solution integrates the observations GNSS position and velocity, $\mathbf{r}^e_{eaG,k}$ and $\mathbf{v}^e_{eaG,k}$; and INS acceleration (forces) and angular velocity, $\mathbf{f}^b_{ib,t}$ and $\boldsymbol{\omega}^b_{ib,t}$. Since both observations must be expressed in the same reference frame, the INS solution must be converted from body to ECEF, which is the preferred reference frame for global positioning solutions. Notice that the GNSS and INS measurement rates may be different.

The fusion algorithm implements an error-state Kalman-Filter (KF), which state transition model is defined by the system, transition and system noise covariance matrices, $\mathbf{F}_{\text{INS},t}$, $\mathbf{\Phi}_{\text{INS},t}$ and $\mathbf{Q}_{\text{INS},t}$, respectively; and the state to be estimated is $\mathbf{x}_{\text{INS},t}$.

In an error-state fusion filter formulation, the main goal is to estimate the position and velocity errors at a given fusion rate t (this will be determined by the lower rate, which in general is given by the GNSS), $\delta\mathbf{r}^e_{eb,t}$ and $\delta\mathbf{v}^e_{eb,t}$, respectively. In addition we can add the attitude error, $\delta\boldsymbol{\psi}^e_{eb,t}$. The KF estimates attitude, velocity and position errors, together with accelerometer and gyro biases, $\mathbf{b}_{a,t}$ and $\mathbf{b}_{g,t}$ (in total 15 states). The INS state (in ECEF coordinates) is given by

$$\mathbf{x}_{\text{INS},t} = [\delta\boldsymbol{\psi}^e_{eb,t}; \delta\mathbf{v}^e_{eb,t}; \delta\mathbf{r}^e_{eb,t}; \mathbf{b}_{a,t}; \mathbf{b}_{g,t}]. \tag{2}$$

We consider the following notation:

- Raw inertial navigation solution: $\tilde{\mathbf{C}}^e_{b,t}$, $\tilde{\mathbf{v}}^e_{eb,t}$, $\tilde{\mathbf{r}}^e_{eb,t}$
- Corrected inertial navigation solution: $\hat{\mathbf{C}}^e_{b,t}$, $\hat{\mathbf{v}}^e_{eb,t}$, $\hat{\mathbf{r}}^e_{eb,t}$
- Raw and corrected inertial solutions are related as: $\hat{\mathbf{C}}^e_{b,t} = (\delta\hat{\mathbf{C}}^e_{b,t})^\top\tilde{\mathbf{C}}^e_{b,t}$, $\hat{\mathbf{v}}^e_{eb,t} = \tilde{\mathbf{v}}^e_{eb,t} - \delta\hat{\mathbf{v}}^e_{eb,t}$ and $\hat{\mathbf{r}}^e_{eb,t} = \tilde{\mathbf{r}}^e_{eb,t} - \delta\hat{\mathbf{r}}^e_{eb,t}$,
- In closed-loop architectures, there is no raw inertial solution, then: $\hat{\mathbf{C}}^e_{b,t} = (\delta\hat{\mathbf{C}}^e_{b,t})^\top\hat{\mathbf{C}}^e_{b,t-1}$, $\hat{\mathbf{v}}^e_{eb,t} = \hat{\mathbf{v}}^e_{eb,t-1} - \delta\hat{\mathbf{v}}^e_{eb,t}$ and $\hat{\mathbf{r}}^e_{eb,t} = \hat{\mathbf{r}}^e_{eb,t-1} - \delta\hat{\mathbf{r}}^e_{eb,t}$

The state or process equation is

$$\mathbf{x}_{\text{INS},t} = \mathbf{\Phi}^e_{\text{INS}}\mathbf{x}_{\text{INS},t-1} + \mathbf{v}^e_{\text{INS},t}, \tag{3}$$

with $\mathbf{v}^e_{\text{INS},t} \sim \mathcal{N}(\mathbf{0}, \mathbf{Q}^e_{\text{INS}})$. The state transition matrix is approximated (first order in $\mathbf{F}\tau_s$) as

$$\mathbf{\Phi}^e_{\text{INS}} \approx \begin{pmatrix} \mathbf{I}_3 - \mathbf{\Omega}^e_{ie}\tau_s & \mathbf{0}_3 & \mathbf{0}_3 & \mathbf{0}_3 & \hat{\mathbf{C}}^e_{b,t}\tau_s \\ \mathbf{F}^e_{21}\tau_s & \mathbf{I}_3 - 2\mathbf{\Omega}^e_{ie}\tau_s & \mathbf{F}^e_{23}\tau_s & \hat{\mathbf{C}}^e_{b,t}\tau_s & \mathbf{0}_3 \\ \mathbf{0}_3 & \mathbf{I}_3\tau_s & \mathbf{I}_3 & \mathbf{0}_3 & \mathbf{0}_3 \\ \mathbf{0}_3 & \mathbf{0}_3 & \mathbf{0}_3 & \mathbf{I}_3 & \mathbf{0}_3 \\ \mathbf{0}_3 & \mathbf{0}_3 & \mathbf{0}_3 & \mathbf{0}_3 & \mathbf{I}_3 \end{pmatrix}$$

where

$$\hat{\mathbf{C}}^e_{b,t} = (\delta\hat{\mathbf{C}}^e_{b,t})^\top \tilde{\mathbf{C}}^e_{b,t} \approx \left(\mathbf{I}_3 - [\delta\hat{\boldsymbol{\psi}}^e_{eb,t}\wedge]\right)\tilde{\mathbf{C}}^e_{b,t}, \quad (4)$$

$$\mathbf{F}^e_{21} = \left[-\left(\hat{\mathbf{C}}^e_{b,t}\hat{\mathbf{f}}^b_{ib,t}\right)\wedge\right], \quad (5)$$

$$\mathbf{F}^e_{23} = -\frac{2\hat{\boldsymbol{\gamma}}^e_{ib}}{r^e_{eS}(\hat{\mathbf{L}}_b)}\frac{(\hat{\mathbf{r}}^e_{eb,t})^\top}{|\hat{\mathbf{r}}^e_{eb,t}|}, \quad (6)$$

with $[\mathbf{a}\wedge]$ representing a skew-symmetric matrix constructed from vector $\mathbf{a}$ (more details in [7]), $r^e_{eS}(\hat{\mathbf{L}}_b)$ the geocentric radius at the Earth's surface as a function of the latitude, and $\hat{\boldsymbol{\gamma}}^e_{ib}$ the gravitational acceleration at the estimated position $\hat{\mathbf{r}}^e_{eb,t}$. The system noise covariance matrix, $\mathbf{Q}^e_{\mathrm{INS}}$, if we have small propagation intervals ($\tau_s < 0.2$ seconds), can be approximated by a block diagonal matrix

$$\mathbf{Q}^e_{\mathrm{INS}} \approx \mathrm{diag}\left(S_{rg}\mathbf{I_3}, S_{ra}\mathbf{I_3}, \mathbf{0}_3, S_{bad}\mathbf{I_3}, S_{bgd}\mathbf{I_3}\right)\tau_s, \quad (7)$$

with $S_{rg} = \sigma^2_{rg}\tau_i$, σ^2_{rg} the variance of the noise on the gyro angular-rate measurements, $S_{ra} = \sigma^2_{ra}\tau_i$, σ^2_{ra} the variance of the noise on the accelerometer specific-force measurements, τ_i the interval between the input of successive accelerometer and gyro outputs to the intertial navigation equations. The bias are statistically characterized by $S_{bad} = \sigma^2_{bad}/\tau_{bad}$ and $S_{bgd} = \sigma^2_{bgd}/\tau_{bgd}$, with σ^2_{bad} and σ^2_{bgd} the variances of the accelerometer and gyro dynamic biases, respectively; τ_{bad} and τ_{bgd} are the correlation times of the dynamic accelerometer and gyro biases.

In the loosely coupled GNSS/INS, the measurement innovation is directly the difference between GNSS position and velocity, and INS position and velocity (at the same rate, which requires the IMU and GNSS to be synchronized to the same time base). The measurement equation is

$$\mathbf{z}_{G,k} = \mathbf{H}^e_G\mathbf{x}_{\mathrm{INS},k} + \mathbf{n}^e_{\mathrm{G},k}, \text{ with } \mathbf{n}^e_{\mathrm{G},k} \sim \mathcal{N}(\mathbf{0}, \mathbf{R}_{\mathrm{G}}), \quad (8)$$

with $\mathbf{z}_{G,k} = [\hat{\mathbf{r}}^e_{eaG,k}, \hat{\mathbf{v}}^e_{eaG,k}]^\top$. The innovation vector is

$$\delta\mathbf{z}^e_{G,k} = \begin{pmatrix} \hat{\mathbf{r}}^e_{eaG,k} - \hat{\mathbf{r}}^e_{eb,k} \\ \hat{\mathbf{v}}^e_{eaG,k} - \hat{\mathbf{v}}^e_{eb,k} \end{pmatrix}, \quad (9)$$

and the measurement matrix can be approximated as

$$\mathbf{H}^e_G \approx \begin{pmatrix} \mathbf{0}_3 & \mathbf{0}_3 & -\mathbf{I}_3 & \mathbf{0}_3 & \mathbf{0}_3 \\ \mathbf{0}_3 & -\mathbf{I}_3 & \mathbf{0}_3 & \mathbf{0}_3 & \mathbf{0}_3 \end{pmatrix}. \quad (10)$$

The measurement noise covariance $\mathbf{R}_{\mathrm{G}} \in \mathbb{R}^2$ must be set according to the error covariance of the GNSS navigation solution.

ACKNOWLEDGMENT

The pilot demonstration was developed in a partnership with: i2CAT, CTTC, UPC, SEAT, Ficosa and Telefónica España.

Part of the development has been supported by the Generalitat de Catalunya through projects 2017 SGR 1479 and 2017 SGR 00376, and the Spanish Government through grants TEC2015-69868-C2-2-R and TEC2016-79988-P.

The authors would like to thank Anna Moragrega, Berta Serracanta, Mar Vidal and Julio C. Barrera for their involvement in the testbed implementation.

REFERENCES

[1] "D4.1 Stand-alone GNSS solutions for ITS," Tech. Rep., Enhanced real time services for an optimised multimodal mobility relying on cooperative networks and open data (TIMON) project, European Union's Horizon 2020 research and innovation programme under grant agreement No 636220, May 2016, https://timon-project.eu/.

[2] "D2.2 Geolocation Referencing Sub-System," Tech. Rep., High precision positioning for Cooperative-ITS applications H2020-636537, July 2016, https://.

[3] "5G Automotive Association," `http://5gaa.org/5g-technology/paving-the-way/`.

[4] "radino32, Technical specifications," `https://shop.in-circuit.de/product_info.php?cPath=22_63&products_id=186`.

[5] J. Arribas, A. Moragrega, C. Fernández-Prades, and P. Closas, "Low-cost GNSS/INS/Odometric sensor fusion platform for ground intelligent transportation systems," in *Proceedings of the ION GNSS 2017, Portland, Oregon (USA)*, September 2017.

[6] J. Arribas, M. Navarro, A. Moragrega, E. Fernández D. Calero, J. Vilà-Valls, and C. Fernández-Prades, "Low-cost GNSS/INS/Odometric sensor fusion platform for ground intelligent transportation systems," in *Proceedings of the ION GNSS 2018, Miami, Florida (USA)*, September 2018.

[7] P. D. Groves, *Principles of GNSS, Inertial, and Multisensor Integrated Navigation Systems, 2nd Ed.*, Artech House, Norwood, United States, 2013.

[8] "CTTC participates in a connected car pilot during the Mobile World Congress," Feb. 2019, http://www.cttc.es/cttc-participates-in-a-connected-car-pilot-during-the-mobile-world-congress/[Online; posted 25/02/2019].